Sustainable Carbon
Materials

https://doi.org/10.48130/scm-0026-0008

Original Research

Catalytic CO_2 desorption from MEA solution using Fe/Zr-modified carbon nanofiber for energy-efficient CO_2 capture

Hesong Li, Yikun Tang, Jianwen Wang, Xi Tang, Shilin Zhao* and Zhiqiang Sun*

Received: 4 December 2025
Revised: 18 January 2026
Accepted: 26 January 2026

Abstract

The high energy demand for solvent regeneration remains a major obstacle to the large-scale deployment of amine-based CO_2 capture. The present study developed Fe- and Zr-modified carbon nanofibers (Fe/Zr-CNF) to catalyze CO_2 desorption from a 5 M monoethanolamine (MEA) solution. Among various carbon supports, CNF showed the highest desorption factor (1.24) and the lowest relative energy consumption (77.2%). Subsequent metal modification yielded a superior catalyst, 10% Fe-CNF, which reduced the relative energy consumption by 14%, and enhanced the desorption factor by 25% compared to CNF. Mechanistic studies indicated that low-valence metal species cooperated with surface oxygenated groups to facilitate HCO_3^- electron transfer, while high-valence metal oxides interacted with Brønsted and Lewis acid sites to promote $MEAH^+$ deprotonation and $MEACOO^-$ dissociation. Furthermore, 10% Fe-CNF exhibited excellent stability after eight regeneration cycles. This work elucidates the synergistic catalytic mechanism of electron transfer and acid site activation, providing a promising strategy for designing efficient catalysts to reduce the energy cost of post-combustion CO_2 capture.

Keywords: CO_2 desorption, MEA, Carbon nanofiber, Iron modification, Catalytic mechanism

Highlights

- 10% Fe-CNF boosted CO_2 desorption by 25%, and cut energy use by 14% in MEA regeneration.
- Low-valence metals aid electron transfer while high-valence oxides create acid sites for deprotonation.
- An optimal acid site ratio in 10% Fe-CNF yielded peak performance and >15% Fe loading blocked active sites.
- The catalyst showed stable performance over eight cycles, combining redox synergy and conductivity to lower energy cost.

---

* Correspondence: Shilin Zhao (slzhao@csu.edu.cn); Zhiqiang Sun (zqsun@csu.edu.cn)
Full list of author information is available at the end of the article.

Graphical abstract

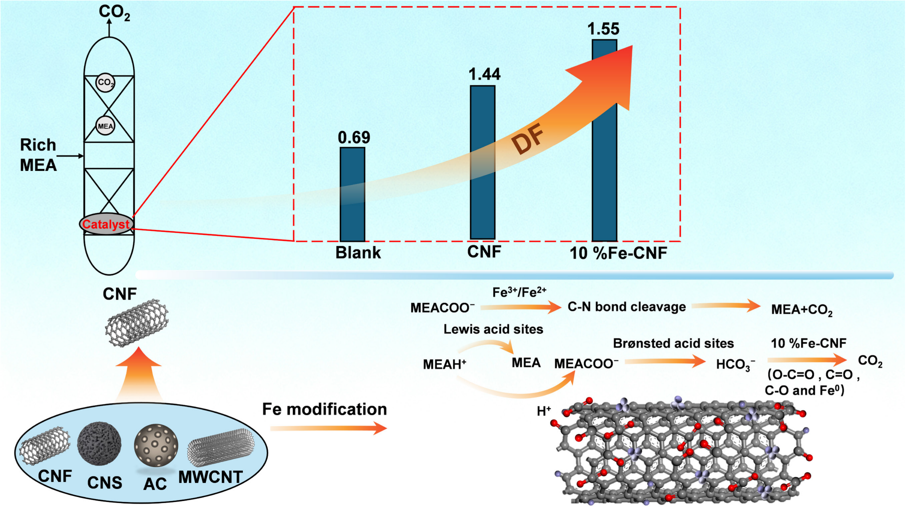

Introduction

Carbon dioxide (CO_2) is widely recognized as the primary greenhouse gas driving global warming and climate change[1,2]. According to projections by the Intergovernmental Panel on Climate Change (IPCC), atmospheric CO_2 concentrations could reach 570 ppm by the year 2100, potentially causing a global average temperature rise of around 1.9 °C and a mean sea-level increase of 3.8 m[3]. In response to this pressing challenge, large-scale carbon capture, utilization, and storage (CCUS) technologies have emerged as crucial strategies for mitigating CO_2 emissions[4]. Among these, post-combustion CO_2 capture via chemical absorption with aqueous alkanolamine solutions, such as monoethanolamine (MEA), is considered one of the most mature and effective approaches[5,6]. However, the high energy demand required for solvent regeneration remains a significant bottleneck hindering its widespread industrial deployment[7,8].

To address this limitation, various catalytic systems have been explored to accelerate amine regeneration and reduce energy consumption. These include carbon-based materials, solid acid catalysts (e.g., zeolites and metal oxides), metal-organic frameworks (MOFs), clay-based materials, and composite catalysts[9,10]. Carbon-based materials have demonstrated remarkable potential in catalytic CO_2 desorption due to their unique electronic properties and tunable surface chemistry. Li et al.[11] demonstrated carbon molecular sieves, porous carbon, carbon nanotubes (CNTs), and graphene could significantly enhance HCO_3^- dehydrogenation through electron transfer, thereby promoting CO_2 desorption. Sp^2-hybridized carbons (such as graphite/graphene) possess highly delocalized π electron systems, which help enhance interactions with CO_2 molecules (for example, through π–π interactions and polarization effects), thereby improving CO_2 adsorption performance and potentially facilitating electron transfer processes[12]. Among them, CNTs particularly exhibited superior performance due to their high surface functionality and large specific surface area, achieving up to a 50% reduction in relative thermal load. Gao et al.[13] further revealed that nitrogen doping introduced both basic and acidic functional groups into CNTs and modified their electronic structure, improving mass transfer from the gas–liquid interface to the bulk MEA solution and increasing the CO_2 desorption rate to 503% of the non-catalytic baseline. The enhanced performance stems from the synergistic effect between the electron-rich nitrogen sites and the carbon matrix, which promotes proton transfer and stabilizes reaction intermediates[14].

Solid acid catalysts, particularly metal oxides, have shown significant promise in amine regeneration. Bhatji et al.[15] reported that the acidic sites of metal oxides facilitated the decomposition of $MEAH^+$ and $MEACOO^-$, improving CO_2 desorption rates by over 30% while reducing thermal load by more than 20%. The mechanism involves Brønsted acid sites protonating the carbamate species, weakening the C–N bond and promoting CO_2 release[16]. Similarly, Tan et al.[17−19] demonstrated that natural clays such as attapulgite, bentonite, and sepiolite possessed intrinsic acidic sites, and metal modification further reduced regeneration energy by over 30% by increasing active site density. Similar enhancements were observed in studies incorporating metals such as Fe, Cu, and Zr into zeolites[20−22] and in Fe-, Ni-, and Ti-modified covalent organic frameworks (COFs) and MOFs, where regeneration energy was reduced by more than 36%[23,24]. These metal species function as Lewis acid sites, accepting electron pairs from the carbamate nitrogen, thereby destabilizing the carbamate complex and facilitating CO_2 desorption.

The combination of metal oxides with carbon materials presents a promising strategy to overcome the limitations of individual components. Metal oxides serve as effective modifiers by introducing strong acidic sites that promote CO_2 desorption, while carbon-based materials offer high surface area, tunable adsorption properties, and excellent stability, making them ideal catalyst supports[25]. The carbon support not only provides a large surface area for metal dispersion but also facilitates electron transfer between the metal sites and the reaction intermediates. This synergistic effect can significantly enhance the catalytic performance by combining the acid-catalyzed decomposition of carbamate species with the electron transfer-promoted dehydrogenation of bicarbonate. Despite these advances, systematic comparisons of different carbon supports in this context remain limited. Although zirconium oxide (ZrO_2) and iron oxide (Fe_2O_3) are known for their strong acidity and have been used in amine regeneration, their practical application is often constrained by non-uniform pore structures and rapid deactivation[22,26]. Therefore, incorporating Zr or Fe oxides into low-valence carbon materials presents a promising strategy, which combines the strong acidic sites of metal oxides with the superior electron transfer capability of carbon substrates to achieve synergistic enhancement in CO_2 desorption performance.

In this work the CO_2 desorption performance of several carbon materials was evaluated, including carbon nanofibers (CNF), carbon nanospheres (CNS), multi-walled carbon nanotubes (MWCNTs), and activated carbon (AC), in a 5 M MEA solution saturated with CO_2 at 98 °C. The most effective carbon support, CNF, was subsequently modified with Fe and Zr in varying loadings to investigate the influence of metal type and content on catalytic performance. Based on experimental results and material characterization, the catalytic desorption mechanism was elucidated. This study aims to provide guidance for the rational design and engineering application of high-performance catalysts for energy-efficient amine-based CO_2 capture.

Materials and methods

Material preparation

The Fe-CNF composite catalyst was prepared via an incipient wetness impregnation method. Specifically, a predetermined amount of $Fe(NO_3)_3{\cdot}9H_2O$ was dissolved in methanol to form a 2.0 mol/L metal salt solution. The CNF support was then impregnated with this solution under continuous magnetic stirring at room temperature for 8 h, followed by an ultrasonic treatment at 40 °C for 0.5 h. The resulting solid was subsequently dried at 120 °C for 14 h. The final catalysts are denoted as y% Fe-CNF, where y represents the nominal mass percentage of Fe. The Zr-CNF catalyst was synthesized following the same procedure, using $ZrOCl_2{\cdot}8H_2O$ as the metal precursor.

Experimental and performance indicators

The CO_2 absorption was performed by bubbling pure CO_2 at 400 mL/min through 200 mL of a 5 M monoethanolamine (MEA) solution at 40 °C and 1 atm. The MEA concentration of 5 M is the optimal choice verified through long-term industrial practice, achieving the best balance between absorption performance, energy consumption, corrosivity, and economy, which has been used commercially for decades[27]. The desorption experiments were conducted in a setup illustrated in Fig. 1. A 200 mL aliquot of the CO_2-rich 5 M MEA solution, containing 2.5 g of catalyst, was loaded into a 500 mL three-neck round-bottom flask. The flask was equipped with a condenser (to minimize amine loss), a thermometer, and a gas inlet. The system was purged with N_2 at 500 mL/min for 10 min to remove air. Desorption was then initiated by heating the solution to 98 °C under vigorous stirring at 1,000 rpm[22]. The outlet gas was dried and scrubbed with concentrated H_2SO_4 before the CO_2 concentration was recorded at 1 min intervals. A wattmeter monitored the energy consumption to calculate the relative desorption energy. The CO_2 loading in the lean solution was determined by titration with 1 M HCl after the desorption.

The catalytic performance for amine regeneration was evaluated based on the CO_2 desorption rate, desorption capacity, and relative thermal load (RH). The desorption factor (DF) was employed as a comprehensive index to reflect the overall catalytic efficiency[13,22,27,28]. The CO_2 desorption rate was calculated according to Eq. (1).

$$V_d = \frac{\dfrac{V_{N_2}\times C^1}{1-C^1}\times\dfrac{273.15}{V_m\times T}}{C\times V} \tag{1}$$

where, V_d is the CO_2 desorption rate (mol/min); V_{N_2} is the N_2 flow rate (0.5 L/min); C^1 is the CO_2 concentration in the outlet gas (%); V_m is the gas molar volume (22.4 L/mol); T is the ambient temperature (K); C is the amine concentration (5 mol/L); and V is the solution volume (0.2 L).

The total amount of CO_2 desorbed within 50 min was determined by Eq. (2).

$$n_d = C\times V\times(\alpha_{rich}-\alpha_{lean}) \tag{2}$$

where, n_d is the total desorbed CO_2 (mol); α_{rich} and α_{lean} are the CO_2 loadings of the rich and lean amine solutions, respectively (mol CO_2/mol MEA), as measured by acid-base titration.

The RH was derived from Eqs (3) and (4).

$$H = \frac{E}{n_d} \tag{3}$$

$$RH = \frac{H_i}{H_b}\times 100\% \tag{4}$$

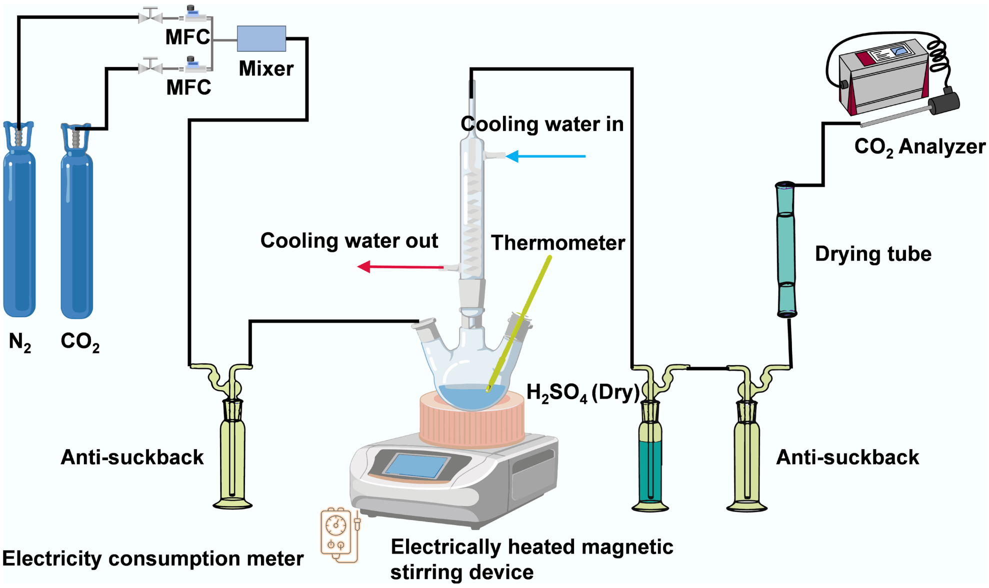

Fig. 1 Schematic diagram of the CO_2 desorption experimental setup.

where, H is the regeneration heat load (kJ/mol); E is the total electrical energy consumed (kJ); H_i and H_b represent the regeneration heat load for the catalytic and blank (non-catalytic) runs, respectively (kJ/mol); RH refers to the relative heat load (%).

Finally, the DF, which comprehensively evaluates the catalytic activity, was calculated using Eq. (5).

$$\mathrm{DF} = \frac{V_d \times n_d}{H_i} \times 100\% \qquad (5)$$

where, DF is the desorption factor, $mol^3/(kJ \cdot min)$.

Characterization methods

The textural properties of the catalysts were determined using N_2 physisorption with a fully automated surface area and porosity analyzer (Micromeritics ASAP 2460). Surface functional groups were characterized by Fourier-transform infrared spectroscopy (FT-IR, Thermo Fisher Nicolet iS20) in the range of 500–4,000 cm^{-1}, while optical properties were analyzed by UV-vis-NIR diffuse reflectance spectroscopy (Shimadzu UV-3600i Plus) from 200 to 800 nm. To elucidate the catalytic mechanism of Fe- and Zr-modified CNF, the chemical states and acidic properties were probed by X-ray photoelectron spectroscopy (XPS, Thermo Scientific K-Alpha) and pyridine-adsorption infrared spectroscopy (Py-IR, Bruker Tensor 27), respectively. For Py-IR analysis, the samples were firstly degassed at 300 °C under vacuum for 2 h, followed by pyridine adsorption and subsequent desorption at 150 °C for 0.5 h. Furthermore, the evolution of surface functional groups on CNF and 10% Fe-CNF during the desorption process was monitored by Raman spectroscopy (Horiba LabRAM HR Evolution).

Results and discussion

CO_2 desorption characteristics of carbon-based carriers

CO_2 desorption tests in a 5 M MEA solution at 98 °C revealed that carbon-based supports significantly enhanced the regeneration performance. As shown in Fig. 2a, the CO_2 desorption rate in the presence of catalysts was markedly higher than that of the blank test during the initial 8 min. While the non-catalytic system attained its maximum desorption rate at 8 min, the CNF-assisted system peaked earlier, at 7 min. Beyond this point, the rate curves of the catalytic and non-catalytic systems converged, which is attributed to the higher residual CO_2 loading in the blank solution compensating for its lower reaction rate constant[11,29]. For a quantitative comparison, the total CO_2 desorption amount, RH, and DF were evaluated over the first 50 min (Fig. 2b). The incorporation of CNS, AC, MWCNT, and CNF increased the CO_2 desorption amount by 24.9%–31.5%, lowered the RH by 13.0%–22.8%, and improved the DF by 56.5%–79.7%. Among all tested materials, CNF exhibited the most outstanding performance, achieving the highest CO_2 desorption amount (107.6 mmol), the lowest RH (77.2%), and the highest DF (1.24).

The surface textural properties of the four carbon supports (CNF, MWCNT, CNS, and AC) are summarized in Table 1. CNS and MWCNT possessed significantly larger specific surface areas and higher micropore volumes than CNF and AC. Despite its modest surface area, CNF demonstrated the best catalytic performance, which suggested that textural parameters were not the sole determining factor. FT-IR spectra (Fig. 2c) showed similar absorption bands at

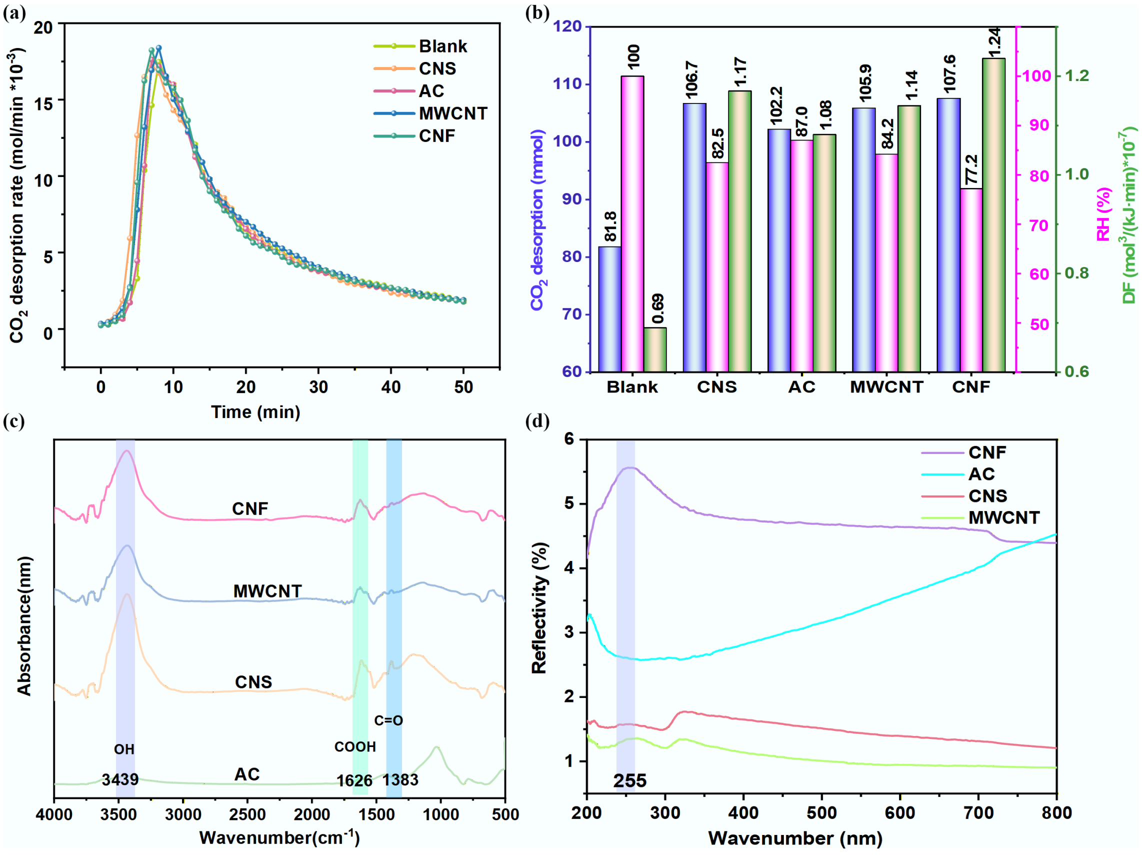

Fig. 2 Catalytic performance and characterization of different carbon materials in CO_2-rich MEA solution. (**a**) CO_2 desorption rate. (**b**) Cumulative desorption amount, RH, and DF after 50 min. (**c**) FT-IR spectra. (**d**) UV-vis.

Table 1 Structural parameters of the carbon materials

Carbon material	BET surface area (m^2/g)	Total pore volume (cm^3/g)	Micropore volume (cm^3/g)
CNS	716.77	0.872	0.228
AC	32.11	0.059	0.005
MWCNT	238.63	1.342	0.028
CNF	19.74	0.027	0.006
10% Fe-CNF	27.79	0.059	0.004
20% Fe-CNF	28.89	0.058	0.004
5% Zr-CNF	22.64	0.049	0.003
20% Zr-CNF	24.91	0.054	0.004

3,439, 1,626, and 1,383 cm^{-1} for all carbon materials, corresponding to -OH, COOH, and C=O, functional groups, respectively[30,31]. The abundance of these oxygen-containing groups on CNF, MWCNT, and CNS (compared to AC) likely contributed to their superior catalytic activity[13]. UV-vis spectra (Fig. 2d) provided further insight, revealing a distinct reflection peak near 255 nm for CNF, MWCNT, and CNS, attributed to $n \rightarrow \pi^*$ and $\pi \rightarrow \pi^*$ transitions[32]. CNF exhibited the highest reflectivity in this region. This high reflectivity will minimize parasitic thermal excitation while preserving strong electron mobility[33], thereby enhancing the catalytic ability of MEA to desorb CO_2. It is consistent with the role of electron transfer in facilitating HCO_3^- desorption and promoting CO_2 release[11]. A parallel was observed in TiO_2 catalysis, which also showed a prominent reflection at 255 nm and effectively reduced regeneration energy despite having a lower surface area than CNF[29,34].

Desorption characteristics of Fe/Zr-loaded CNF

Given its superior performance among the carbon-based catalysts, CNF was selected as the support for metal modification with Fe and Zr. Figure 3a shows that all Fe-CNF catalysts enhanced the CO_2 desorption rate compared to pristine CNF during the initial 8 min, with 20% Fe-CNF exhibiting the most pronounced effect. Between 8 and 11 min, the 5%–15% Fe-CNF samples maintained excellent activity, after which the rates converged across all systems. As summarized in Fig. 3b, Fe modification reduced the RH by 13.9%–36.9% and increased the DF by 0.81%–25%, compared to the CNF. However, only the 10% Fe-CNF catalyst increased the total CO_2 desorption amount (by 2.0 mmol), whereas higher loadings, particularly 20% Fe-CNF, led to a significant decrease, resulting in a desorption amount (83.4 mmol) close to the blank test and a DF of only 1.23. This decline is likely due to the rapid depletion of MEACOO in the early stage[35–37]. Beyond 11 min, the thermal energy at 98 °C became insufficient to drive further decomposition at low MEACOO concentrations, thereby lowering cumulative desorption. In contrast, Zr-CNF catalysts (Fig. 3c) showed varying performance: 5% and 10% loadings reduced CO_2 desorption amounts by 17.9% and 8.7%, respectively, while 20% Zr-CNF exhibited a high desorption rate between 8–13 min, similar to 10% Fe-CNF. Although Zr modification also lowered the RH by 12.6%–29% compared to the CNF (Fig. 3d), the accompanying drop in desorption capacity yielded a lower overall DF than Fe-CNF. In summary, both Fe and Zr modifications enhanced the catalytic desorption performance of CNF, but the metal loading level critically influenced the outcome. This dependence is likely associated with metal-induced changes in surface functional groups, specific surface area, and acidic site density[28].

The DF serves as the key metric for evaluating the catalytic performance of metal-modified CNF. To elucidate the structure-activity relationship, 10% Fe-CNF (highest DF) and 20% Fe-CNF (lowest DF) among the Fe series, along with 5% Zr-CNF (lowest DF) and 20% Zr-CNF (highest DF) among the Zr series, were selected for detailed characterization. As summarized in Table 1, metal incorporation generally increases the specific surface area of CNF, with 20% Fe-CNF showing the most significant enhancement (46.4%). The total pore volume was also improved, most notably in 10% Fe-CNF (118.5% increase). FT-IR spectra (Fig. 3e) revealed that the main

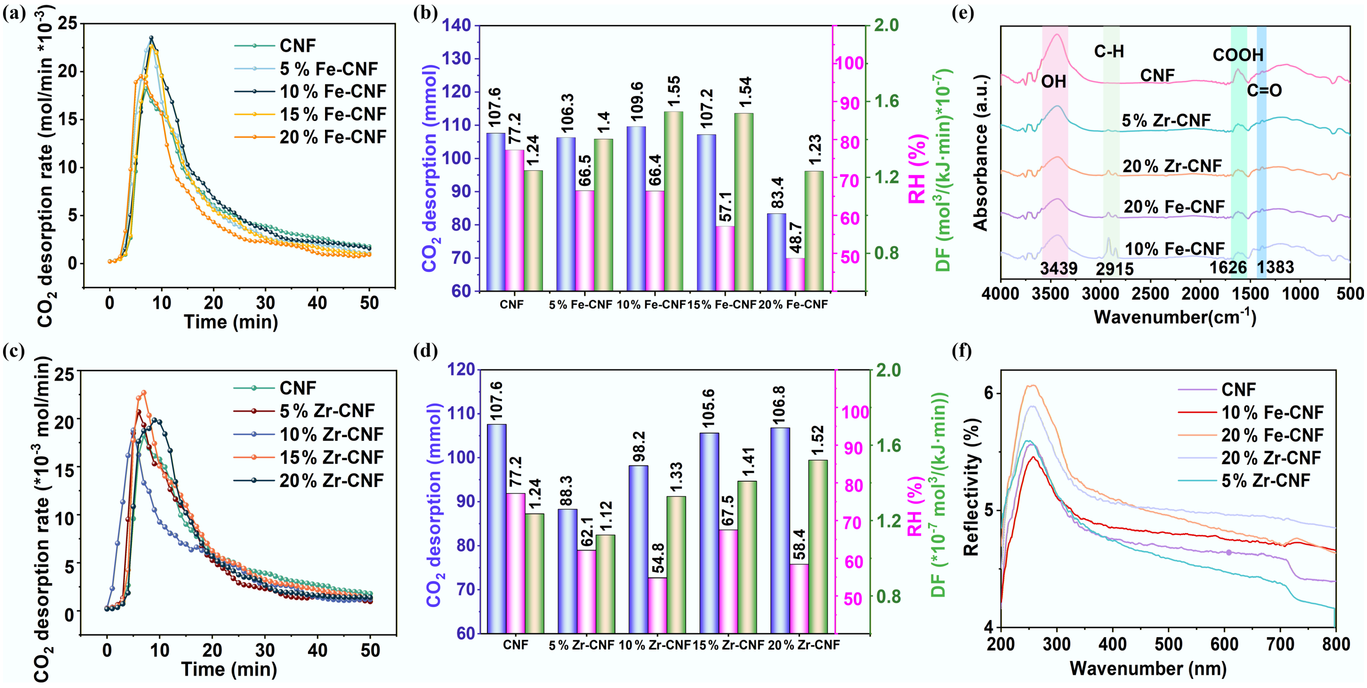

Fig. 3 Catalytic desorption performance of CO_2-rich MEA solution with Fe- and Zr-modified CNF. (**a**), (**c**) Desorption rate of Fe/Zr-CNF. (**b**), (**d**) Desorption amount, RH, and DF of Fe/Zr-CNF. Characterization of catalytic desorption of CO_2-rich MEA solution with Fe- and Zr-modified CNF. (**e**) FT-IR. (**f**) UV-vis.

framework of CNF remained largely unchanged after metal modification. However, a new absorption band emerged at approximately 2,915 cm^{-1}, which was assigned to the C–H stretching vibration of residual surfactant molecules[22]. UV-vis spectra (Fig. 3f) showed a substantial increase in reflectivity for catalysts with 20% metal loading. This was attributed to the higher surface concentration of metal species and potential changes in the size of surface metal clusters[38]. These findings collectively indicated that Fe and Zr introduction not only modified surface functional groups but also influenced catalytic performance by altering the dispersion and morphology of metal particles on the CNF surface[22].

XPS analysis revealed the distinct effects of Fe and Zr modification on the surface chemistry of CNF (Fig. 4a–f)[22,39]. Deconvolution of the C 1s spectra showed characteristic peaks for C–C (284.8 eV), C–O (286.1 eV), and C=O (289.0 eV) (Fig. 4a, d)[40,41]. In the O 1s spectra, pristine CNF exhibited peaks corresponding to O–C=O (531.1 eV), C–O (532.6 eV), and adsorbed C=O (534.0 eV) (Fig. 4b, e)[22,42]. Metal modification significantly altered these oxygen species: Fe-CNF showed a sharp increase in O–C=O content with a concurrent decrease in C=O, whereas Zr-CNF exhibited a reduction in both C=O and O–C=O alongside an increase in C–O. These trends suggest different metal-support interaction mechanisms, likely due to the preferential coordination of Fe^{3+} with carboxyl groups and Zr^{4+} with hydroxyl groups[43]. In Fe-CNF catalysts, the Fe 2p spectra (Fig. 4c) confirmed the presence of octahedrally coordinated Fe^{3+}, indicated by a peak separation exceeding 13 eV between Fe $2p_{3/2}$ and Fe $2p_{1/2}$[22,44]. A satellite peak at 714.2 eV was assigned to tetrahedral Fe^{3+}, while a feature at 706.5 eV corresponded to metallic Fe^0[45]. Notably, 10% Fe-CNF possessed a higher relative content of Fe^0 than 20% Fe-CNF, which may contribute to its superior catalytic performance due to the provision of more possibilities for electron transfer[36]. For Zr-CNF, the Zr 3d spectra (Fig. 4f) indicated that Zr exists predominantly as Zr^{4+}[22,46,47]. The proportion of high-valence metal species (Fe^{3+}, Zr^{4+}) increased with metal loading and correlates with a reduction in regeneration heat duty, suggesting that these sites facilitate energy efficiency by accepting lone pair electrons from carbamate nitrogen, thereby promoting C–N bond cleavage[32,36]. However, the excellent performance of 10% Fe-CNF and 15% Zr-CNF also indicated that low-valence species (such as Fe^{2+}, Zr^{2+}, and Fe^0) could reduce the activation energy of CO_2 desorption through electronic effects, geometric effects, and synergistic effects, which played a key role in enhancing the CO_2 desorption rate. The overall catalytic performance was governed by a synergistic interplay between low-valence species, which boosted the desorption rate, and high-valence oxides, which primarily lowered the energy barrier[22].

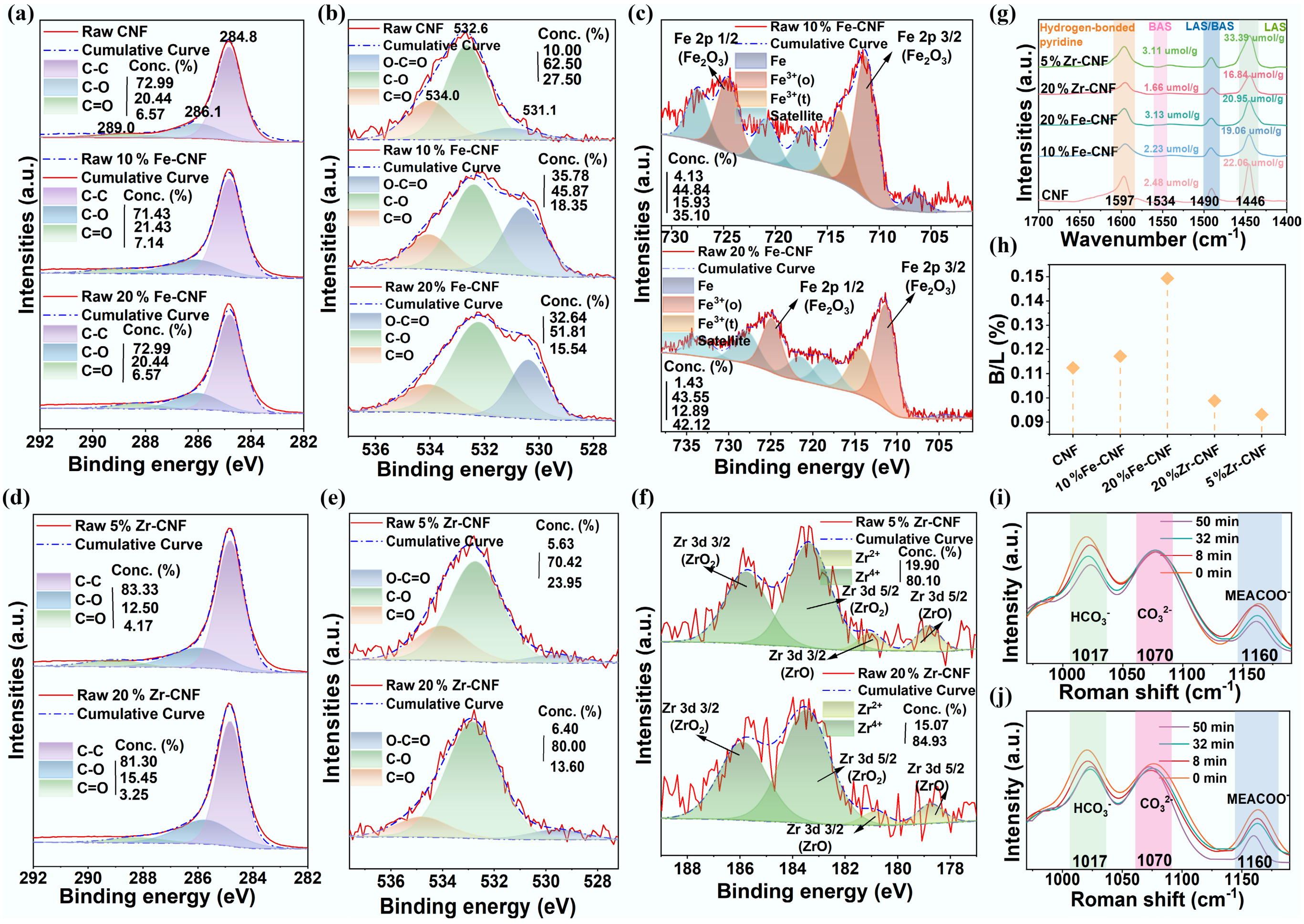

Fig. 4 XPS and Py-IR characterization of the catalysts, and *in situ* Raman monitoring of the desorption process. (**a**)–(**c**) XPS spectra of C 1s, O 1s, and Fe 2p for CNF, 10% Fe-CNF, and 20% Fe-CNF. (**d**)–(**f**) XPS spectra of C 1s, O 1s, and Zr 3d for 5% Zr-CNF and 20% Zr-CNF. (**g**) Py-IR spectra. (**h**) Brønsted (B)/Lewis (L) acid sites ratios. *In situ* Raman spectra of the CO_2-rich MEA solution during desorption (**i**) without a catalyst, and (**j**) with 10% Fe-CNF.

The surface acidity of the catalysts, quantified by pyridine-adsorption infrared (Py-IR) spectroscopy, revealed distinct differences in Brønsted and Lewis acid site distributions (Fig. 4g). Characteristic peaks at 1,446 cm^{-1} (Lewis acid site), 1,534 cm^{-1} (Brønsted acid site), 1,490 cm^{-1} (Brønsted and Lewis acid site), and 1,597 cm^{-1} (hydrogen-bonded pyridine) were observed[21,22]. Compared with pristine CNF, Zr-modified catalysts generally showed increased Brønsted acid site content, whereas Fe-modified catalysts exhibited a decrease. In particular, Lewis acid site content increased only for 5% Zr-CNF and 20% Fe-CNF but decreased for all other metal-loaded samples. Consequently, the Brønsted/Lewis ratio increased for Fe-CNF but decreased for Zr-CNF (Fig. 4h). Comparing the raw CNF, 10% Fe-CNF, and 20% Fe-CNF, it showed that the Brønsted/Lewis (B/L) acid site ratio increased with the increase in Fe loading. However, 10% Fe-CNF exhibited the optimal desorption effect, indicating that the catalytic effect was not simply linearly related to the Brønsted/Lewis (B/L) acid site ratio. These acid sites play complementary roles in catalyzing CO_2 desorption: Brønsted acid site provides protons that facilitate MEACOO$^-$ cleavage, while Lewis acid site acts as a proton acceptor to promote MEAH$^+$ deprotonation[18,21,48]. Their synergistic interaction enhances the overall conversion efficiency of key amine species. *In situ* Raman spectroscopy further elucidated the reaction pathway promoted by 10% Fe-CNF (Fig. 4i, j). Characteristic peaks at 1,017 cm^{-1} (C–OH in HCO_3^-), 1,070 cm^{-1} (C–O in CO_3^{2-}), and 1,160 cm^{-1} (C–N in MEACOO$^-$) were monitored[11,23,49]. In the non-catalytic system, HCO_3^- decomposed rapidly during the initial heating stage (0–8 min), while MEACOO$^-$ remained stable until higher temperatures (8–50 min)[7,8]. In contrast, the presence of 10% Fe-CNF induced a marked decrease in the MEACOO$^-$ peak intensity as early as 8 min, confirming its efficacy in promoting carbamate decomposition at low temperature. Notably, between 32 and 50 min, the HCO_3^- peak area increased concurrently with the decrease in MEACOO$^-$, suggesting a possible interconversion between these species during the catalyzed desorption process.

Catalytic desorption cyclic stability of 10% Fe-CNF

For industrial deployment, a viable catalyst must possess not only high activity but also robust stability. To evaluate this, the 10% Fe-CNF catalyst was recovered after each desorption cycle via washing, filtration, and drying at 120 °C for 10 h. Minor mass losses were compensated for by supplementing fresh catalyst to maintain a constant total mass of 2.5 g for subsequent tests. As shown in Fig. 5, the catalyst maintained stable performance over eight consecutive cycles. The RH showed no significant increase (maximum variation within 13.1%), while the CO_2 desorption capacity exhibited no appreciable decline (maximum difference of 14 mmol). These results confirmed the excellent cyclic stability of 10% Fe-CNF. Consequently, 10% Fe-CNF demonstrated strong potential for industrial application in amine-based CO_2 capture processes.

Catalytic desorption mechanism

CO_2 absorption by MEA typically proceeds via the two-step zwitterion mechanism or the single-step bicarbonate mechanism, respectively[11]. In the zwitterion route, CO_2 initially reacts with MEA to form a zwitterionic intermediate (MEA$^+$COO$^-$), which subsequently reacts with another MEA molecule, yielding MEACOO$^-$ and MEAH$^+$. In the bicarbonate pathway, H_2O directly participates in the reaction, leading to the formation of HCO_3^- and MEAH$^+$. As illustrated in Fig. 6, the catalytic mechanism of 10% Fe-CNF involved multiple synergistic effects. Firstly, high-valent metal oxides attack oxygen atoms. A chemisorption process then occurred between oxygen and metal atoms, accompanied by an isomerization step where protons were transferred from O to N atoms. Protons subsequently abstracted the lone-pair electrons of N atoms. The hybridization of N atoms shifted from sp^2 to sp^3. The strength of the C–N bond weakened due to stretching. Furthermore, metal atoms or metal oxides further attacked N atoms and helped stretch the C–N bond, enhancing CO_2 desorption performance. The C–N bond thus broke, and the zwitterion decomposed into MEA and CO_2. Secondly, Lewis acid sites participate in the deprotonation of MEAH$^+$, transferring protons from MEAH$^+$ to MEACOO$^-$. Brønsted acid sites directly participated in the dissociation of MEACOO$^-$. The unique structure of the 10% Fe-CNF catalyst accelerated mass transfer between the catalyst and the solution. Low-valent Fe atoms, in combination with surface functional groups (O–C=O, –C=O, C–O), jointly promoted electron transfer of HCO_3^-, leading to an increase in CO_2 desorption capacity[22,36].

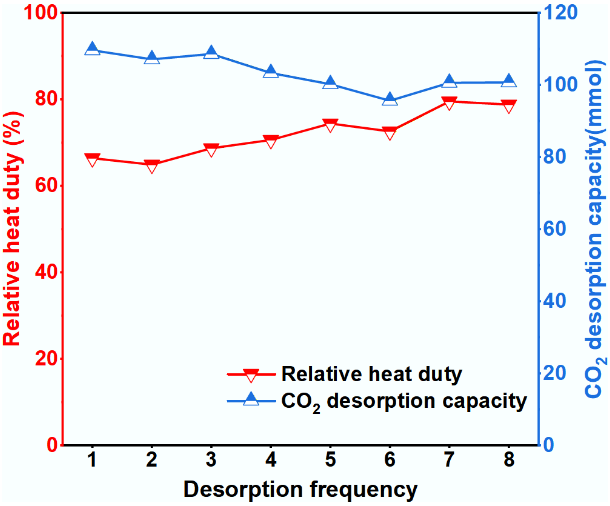

Fig. 5 Cyclic stability evaluation of the 10% Fe-CNF catalyst over eight adsorption-desorption cycles.

Conclusions

Among the carbon-based materials evaluated, CNF demonstrated superior catalytic performance for CO_2 desorption in 5 M MEA, which increased the desorption amount by 31.5% and reduced the RH by 22.8% compared to the non-catalytic system. Metal modification further improved the regeneration efficiency, with 10% Fe-CNF achieving the highest DF (1.55×10^{-3} mol^3/(kJ·min)). However, Fe loadings exceeding 15% led to partial blockage of active sites and diminished performance. The incorporation of Fe^{3+} or Zr^{4+} created synergistic Brønsted and Lewis acid sites that promoted MEACOO$^-$ decomposition and MEAH$^+$ deprotonation. The optimal acid site distribution, reflected in the B/L ratio of 10% Fe-CNF, was crucial for maximizing desorption efficiency. Moreover, low-valence metal species (e.g., Fe^0, Zr^{2+}) enhanced electron transfer and facilitated HCO_3^- dehydrogenation, while high-valence metal oxides (e.g., Fe^{3+}, Zr^{4+}) stabilized key intermediates and reduced the reaction activation energy. The combined effect of redox synergy and the high conductivity of CNF collectively lowered the energy barrier for MEA regeneration. This work elucidates a dual catalytic mechanism involving acidic site activation

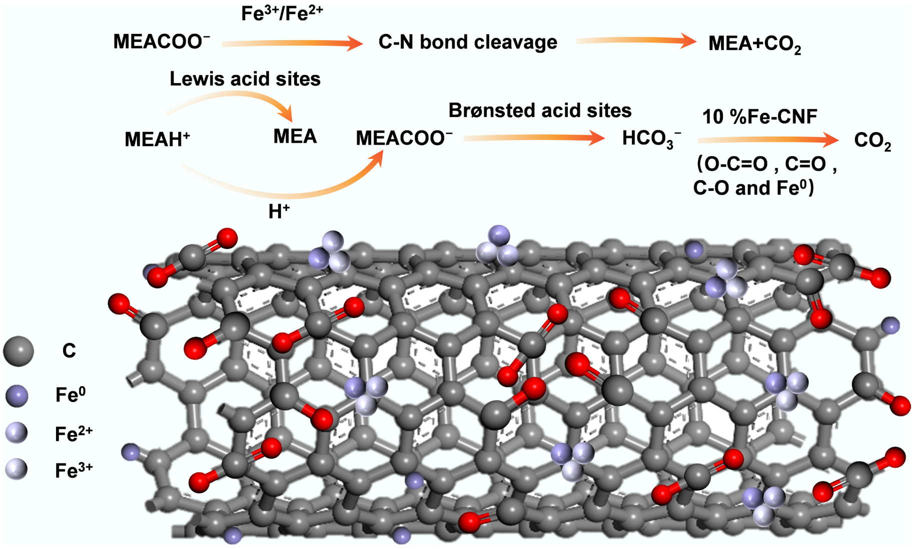

Fig. 6 Catalytic mechanism of 10% Fe-CNF for CO_2 desorption from MEA solution.

and electron transfer synergy in Fe/Zr-CNF catalysts, providing theoretical and practical foundations for designing efficient, energy-saving catalysts for amine-based CO_2 capture.

Author contributions

The authors confirm their contributions to the paper as follows: Hesong Li: writing – original draft, writing – review & editing, supervision, methodology, investigation, funding acquisition, data curation, conceptualization; Yikun Tang: writing – review & editing, software; Jianwen Wang: investigation, software, experiment, data curation, writing – review & editing; Xi Tang: writing – review & editing, software; Shilin Zhao: conceptualization, writing – review & editing. Zhiqiang Sun: Conceptualization, writing – review & editing. All authors reviewed the results and approved the final version of the manuscript.

Data availability

The datasets used or analyzed during the current study are available from the corresponding author upon reasonable requests.

Funding

This work was financially supported by the Science and Technology Innovation Program of Hunan Province (Grant No. 2023RC3043), the Natural Science Foundation of Hunan Province (Grant No. 2025JJ50278), and the High Performance Computing Center of Central South University.

Declarations

Competing interests

The authors declare that they have no conflict of interest.

Author details

Hunan Engineering Research Center of Clean and Low-Carbon Energy Technology, School of Energy Science and Engineering, Central South University, Changsha 410083, China

References

[1] Wei YM, Kang JN, Liu LC, Li Q, Wang PT, et al. 2021. A proposed global layout of carbon capture and storage in line with a 2 °C climate target. *Nature Climate Change* 11:112−118

[2] Gao W, Liang S, Wang R, Jiang Q, Zhang Y, et al. 2020. Industrial carbon dioxide capture and utilization: state of the art and future challenges. *Chemical Society Reviews* 49:8584−8686

[3] Song C, Liu Q, Deng S, Li H , Kitamura Y. 2019. Cryogenic-based CO_2 capture technologies: state-of-the-art developments and current challenges. *Renewable and Sustainable Energy Reviews* 101:265−278

[4] Jiang K, Li K, Puxty G, Yu H, Feron PHM. 2018. Information derivation from vapor-liquid equilibria data: a simple shortcut to evaluate the energy performance in an amine-based postcombustion CO_2 capture. *Environmental Science & Technology* 52:10893−10901

[5] Meng F, Meng Y, Ju T, Han S, Lin L, et al. 2022. Research progress of aqueous amine solution for CO_2 capture: a review. *Renewable and Sustainable Energy Reviews* 168:112902

[6] Zhang X, Zhang S, Tan Z, Zhao S, Peng Y, et al. 2023. One-step synthesis of efficient manganese-based oxide catalyst for ultra-rapid CO_2 absorption in MDEA solutions. *Chemical Engineering Journal* 465:142878

[7] Zhou X, Li X, Wei J, Fan Y, Liao L, et al. 2020. Novel nonaqueous liquid-liquid biphasic solvent for energy-efficient carbon dioxide capture with low corrosivity. *Environmental Science & Technology* 54:16138−16146

[8] Chen Z, Yuan B, Zhan G, Li Y, Li J, et al. 2022. Energy-efficient biphasic solvents for industrial carbon capture: role of physical solvents on CO_2 absorption and phase splitting. *Environmental Science & Technology* 56:12785−13516

[9] Aghel B, Janati S, Wongwises S, Shadloo MS. 2022. Review on CO_2 capture by blended amine solutions. *International Journal of Greenhouse Gas Control* 119:103715

[10] Bhatti AH, Waris M, Kazmi WW, Bhatti UH, Min GH, et al. 2023. Metal impregnated activated carbon as cost-effective and scalable catalysts for amine-based CO_2 capture. *Journal of Environmental Chemical Engineering* 11:109231

[11] Li X, Xu Q, Liu Z, Chen J, Xie HB, et al. 2023. Nonacid carbon materials as catalysts for monoethanolamine energy-efficient regeneration. *Environmental Science & Technology* 57:9975−9983

[12] Mehra P, Paul A. 2022. Decoding carbon-based materials'properties for high CO_2 capture and selectivity. *ACS Omega* 7:33637−34709

[13] Gao Y, He X, Mao K, Russell CK, Toan S, et al. 2023. Catalytic CO_2 capture via ultrasonically activating dually functionalized carbon nanotubes. *ACS Nano* 17:8345−8354

[14] Sun X, Li F, Xu Y, Zhang Q, Ma J. 2025. A review on N-doped carbon-based materials for the NH_3-SCR reaction. *Nanomaterials* 15:1544

[15] Bhatti UH, Kazmi WW, Min GH, Haider J, Nam S, et al. 2021. Facilely synthesized M-montmorillonite (M = Cr, Fe, and Co) as efficient catalysts for enhancing CO_2 desorption from amine solution. *Industrial & Engineering Chemistry Research* 60:13318−13325

[16] Li T, Yu Q, Barzagli F, Li CE, Che M, et al. 2023. Energy efficient catalytic CO_2 desorption: mechanism, technological progress and perspective. *Carbon Capture Science & Technology* 6:100099

[17] Tan Z, Zhang S, Zhao F, Zhang R, Tang F, et al. 2023. SnO_2/ATP catalyst enabling energy-efficient and green amine-based CO_2 capture. *Chemical Engineering Journal* 453:139801

[18] Tan Z, Zhang S, Yue X, Zhao F, Xi F, et al. 2022. Attapulgite as a cost-effective catalyst for low-energy consumption amine-based CO_2 capture. *Separation and Purification Technology* 298:121577

[19] Tan Z, Zhang X, Zhang S, Peng Y, Zhao S, et al. 2024. Enhancing CO_2 desorption rate in rich MEA solutions by metal-modified attapulgite catalyst. *Separation and Purification Technology* 330:125513

[20] Zhang R, Li T, Zhang Y, Ha J, Xiao Y, et al. 2022. CuO modified KIT-6 as a high-efficiency catalyst for energy-efficient amine solvent regeneration. *Separation and Purification Technology* 300:121702

[21] Zhang X, Huang Y, Yang J, Gao H, Huang Y, et al. 2020. Amine-based CO_2 capture aided by acid-basic bifunctional catalyst: advancement of amine regeneration using metal modified MCM-41. *Chemical Engineering Journal* 383:123077

[22] Zhang X, Zhu Z, Sun X, Yang J, Gao H, et al. 2019. Reducing energy penalty of CO_2 capture using Fe promoted SO_4^{2-}/ZrO_2/MCM-41 catalyst. *Environmental Science & Technology* 53:6094−6102

[23] Xing L, Wei K, Li Y, Fang Z, Li Q, et al. 2021. TiO_2 coating strategy for robust catalysis of the metal-organic framework toward energy-efficient CO_2 capture. *Environmental Science & Technology* 55:11216−11224

[24] Li Y, Chen Z, Zhan G, Yuan B, Wang L, et al. 2022. Inducing efficient proton transfer through Fe/Ni@COF to promote amine-based solvent regeneration for achieving low-cost capture of CO_2 from industrial flue gas. *Separation and Purification Technology* 298:121676

[25] Wang W, Song Q, Luo Q, Li L, Huo X, et al. 2023. Photothermal-enabled single-atom catalysts for high-efficiency hydrogen peroxide photosynthesis from natural seawater. *Nature Communications* 14:2493

[26] Liu H, Zhang X, Gao H, Liang Z, Idem R, et al. 2017. Investigation of CO_2 regeneration in single and blended amine solvents with and without catalyst. *Industrial & Engineering Chemistry Research* 56:7656−7664

[27] Zhang X, Zhang X, Liu H, Li W, Xiao M, et al. 2017. Reduction of energy requirement of CO_2 desorption from a rich CO_2-loaded MEA solution by using solid acid catalysts. *Applied Energy* 202:673−684

[28] Zhang X, Zhang R, Liu H, Gao H, Liang Z. 2018. Evaluating CO_2 desorption performance in CO_2-loaded aqueous tri-solvent blend amines with and without solid acid catalysts. *Applied Energy* 218:417−429

[29] Bhatti UH, Shah AK, Kim JN, You JK, Choi SH, et al. 2017. Effects of transition metal oxide catalysts on MEA solvent regeneration for the post-combustion carbon capture process. *ACS Sustainable Chemistry & Engineering* 5:5862−5868

[30] Alivand MS, Mazaheri O, Wu Y, Zavabeti A, Christofferson AJ, et al. 2022. Engineered assembly of water-dispersible nanocatalysts enables low-cost and green CO_2 capture. *Nature Communications* 13:1249

[31] Li MF, Liu YG, Liu SB, Shu D, Zeng GM, et al. 2017. Cu(II)-influenced adsorption of ciprofloxacin from aqueous solutions by magnetic graphene oxide/nitrilotriacetic acid nanocomposite: competition and enhancement mechanisms. *Chemical Engineering Journal* 319:219−228

[32] Georgakilas V, Perman JA, Tucek J, Zboril R. 2015. Broad family of carbon nanoallotropes: classification, chemistry, and applications of fullerenes, carbon dots, nanotubes, graphene, nanodiamonds, and combined superstructures. *Chemical Reviews* 115:4744−4822

[33] Banal JL, Zhang B, Jones DJ, Ghiggino KP, Wong WWH. 2017. Emissive molecular aggregates and energy migration in luminescent solar concentrators. *Accounts of Chemical Research* 50:49−57

[34] Liu L, Chen X. 2014. Titanium dioxide nanomaterials: self-structural modifications. *Chemical Reviews* 114:9890−9918

[35] Lu S, Xue Y, Meng F, Liu M, Hou T, et al. 2025. *In-situ* synthesis of Fe-MOR molecular sieve catalyst for energy-efficient CO_2 capture. *Carbon Capture Science & Technology* 15:100433

[36] Rao L, Jin B, Chen D, Jin X, Liu G, et al. 2024. Energy-saving CO_2 desorption from amine solution over Fe/SiO_2/biochar catalysts: desorption performance, structure-activity relationship, and mechanism. *Chemical Engineering Journal* 483:149413

[37] Zhou Z, Zheng J, Shao L, Zhang X, Pan C, et al. 2025. Ni/Fe-loaded mesoporous KIT-6 enhanced proton transfer for efficient CO_2 desorption. *Chemical Engineering Journal* 522:167863

[38] Sakthivel S, Shankar MV, Palanichamy M, Arabindoo B, Bahnemann DW, et al. 2004. Enhancement of photocatalytic activity by metal deposition: characterisation and photonic efficiency of Pt, Au and Pd deposited on TiO_2 catalyst. *Water Research* 38:3001−3008

[39] Liu R, Liu R, Ma X, Davis BH, Li Z. 2018. Efficient diesel production over the iron-based Fischer-Tropsch catalyst supported on CNTs treated by urea/NaOH. *Fuel* 211:827−836

[40] Liu XM, Romero HE, Gutierrez HR, Adu K, Eklund PC. 2008. Transparent boron-doped carbon nanotube films. *Nano Letters* 8:2613−2619

[41] Ud Din I, Shaharun MS, Subbarao D, Naeem A. 2016. Surface modification of carbon nanofibers by HNO_3 treatment. *Ceramics International* 42:966−970

[42] Yoon CM, Long D, Jang SM, Qiao W, Ling L, et al. 2011. Electrochemical surface oxidation of carbon nanofibers. *Carbon* 49:96−105

[43] You X, Wu H, Zhang R, Su Y, Cao L, et al. 2019. Metal-coordinated sub-10 nm membranes for water purification. *Nature Communications* 10:4160

[44] Yang J, Zhao Y, Liang S, Zhang S, Ma S, et al. 2018. Magnetic iron–manganese binary oxide supported on carbon nanofiber ($Fe_{3-x}Mn_xO_4$/CNF) for efficient removal of Hg^0 from coal combustion flue gas. *Chemical Engineering Journal* 334:216−224

[45] Dong L, Zang J, Wang W, Liu X, Zhang Y, et al. 2020. Electrospun single iron atoms dispersed carbon nanofibers as high performance electrocatalysts toward oxygen reduction reaction in acid and alkaline media. *Journal of Colloid and Interface Science* 564:134−142

[46] Luo J, Luo X, Crittenden J, Qu J, Bai Y, et al. 2015. Removal of antimonite (Sb(III)) and antimonate (Sb(V)) from aqueous solution using carbon nanofibers that are decorated with zirconium oxide (ZrO_2). *Environmental Science & Technology* 49:11115−11124

[47] Fang R, Xu R, Zhang L, Sun X, Wang Y, et al. 2022. Polarization structural design in core–shell fillers: an approach to significantly enhance the energy storage properties of BST/PVDF composite films. *ACS Applied Electronic Materials* 4:2534−2544

[48] Idem R, Shi H, Gelowitz D, Tontiwachwuthikul P. 2017. *U. S. Catalytic method and apparatus for separating a gaseous component from an incoming gas stream. WO Patent No. US9586175*

[49] Lai Q, Toan S, Assiri MA, Cheng H, Russell AG, et al. 2018. Catalyst-$TiO(OH)_2$ could drastically reduce the energy consumption of CO_2 capture. *Nature Communications* 9:2672